Original Article

Institution of MECHANICAL ENGINEERS

Journal of ENGINEERING FOR THE MARITIME ENVIRONMENT

Proc IMechE Part M:
J Engineering for the Maritime Environment
2024, Vol. 238(2) 406–416
© IMechE 2023
Article reuse guidelines:
sagepub.com/journals-permissions
DOI: 10.1177/14750902231196812
journals.sagepub.com/home/pim
Sage

Determination of particle paths and hydrodynamic forces of random wind forced nonlinear ocean waves

Marten Hollm[1], Leo Dostal[1], John D Carter[2] and Robert Seifried[1]

Abstract

The hydrodynamic forces of nonlinear deep water gravity waves acting on cylindrical offshore structures are studied. Thereby, the waves are excited by random wind and the corresponding effect on the particle paths and hydrodynamic forces is investigated. This is done for the Peregrine breather solution of the nonlinear Schrödinger equation, which is nowadays considered as a prototype of extreme waves in open seas. Using this theory, the loads on mechanical structures can be calculated efficiently. It is shown that the Peregrine breather can exist under strong and gusty wind conditions and the water particles experience a horizontal drift. This leads to a force with randomly increasing amplitude in time, whereby a mean wind velocity of 50 km/h results in an increase of about 3%. The increase of hydrodynamic forces caused by the wind should therefore be considered for the construction of mechanical structures operating in the ocean.

Keywords

Nonlinear Schrödinger equation, irregular sea, hydrodynamic forces, particle trajectories, cylindrical offshore structures

Date received: 13 June 2023; accepted: 5 August 2023

Introduction

For the construction of mechanical structures operating in the ocean, appropriate safety limits have to be determined. Therefore, the magnitude and temporal behavior of the hydrodynamic forces acting on mechanical structures occurring in the ocean have to be investigated. In order to model the forces as realistically as possible, the corresponding water waves have to be modeled appropriately. Random wind and the occurrence of extreme waves should therefore be taken into account.

For the study of the behavior of extreme waves in the presence of random wind forcing, Dias et al.[1] have shown that instead of considering the Navier-Stokes equations it is sufficient to use the Euler equations of fluid dynamics. Since the Euler equations contain boundary conditions at the unknown sea surface, the calculation of a numerical solution is not efficient. However, Zakharov[2] has shown that solutions of the Euler equations can be reduced to solutions of the nonlinear Schrödinger equation (NLS). The NLS can be solved much more efficiently than the Euler equations. It has been shown that analytical solutions of the NLS describe very well the behavior of ocean waves with a small steepness.[3] Thus, the NLS has been found to capture very well the dynamics of the wave field to generate extreme waves.[4] This includes especially complex phenomena such as modulation instability, also known as sideband instability. Furthermore, the behavior of extreme waves can be described by weakly nonlinear equations.[5,6]

Later, Leblanc[7] has extended the NLS by a constant unidirectional wind forcing. In order to model the effects of wind excitation as realistically as possible, Dostal et al.[8] have used a random wind forcing in their calculations. Thereby, they have shown that specific solutions of the NLS like the Peregrine breather can

[1]Institute of Mechanics and Ocean Engineering, Hamburg University of Technology, Hamburg, Germany
[2]Mathematics Department, Seattle University, Seattle, WA, USA

Corresponding author:
Marten Hollm, Institute of Mechanics and Ocean Engineering, Hamburg University of Technology, Eissendorfer Strasse 42, Hamburg 20173, Germany.
Email: marten.hollm@tuhh.de

exist in the presence of random wind forcing. Although the structure of the Peregrine is not destroyed by random wind, it is not clear how the water particle trajectories and hydrodynamic forces acting on mechanical structures are influenced by wind.

In order to answer this question, the wave kinematics have to be calculated. For this, the velocity potential corresponding to the water waves has to be computed. Carter et al.[9] have shown how the velocity potential can be calculated if the wave envelope of the solution of the NLS is known.

This work is an extended version of the work of Hollm et al.[10] The effects of random wind on water particle trajectories and hydrodynamic forces acting on mechanical structures are investigated and presented. Considering the Peregrine breather solution of the NLS, which can be seen as a prototype of rogue waves, water particle trajectories and hydrodynamic loads resulting from extreme waves are determined in a very efficient way in this work. Moreover, it is considered how the trajectories and loads change for different types of random wind excitation. Thereby, the forces are computed for the case of a cylindrical pile using the equation presented by Morison et al.[11]

The work is organized as follows: First of all, the NLS is introduced for the modeling of nonlinear dissipative waves excited by random wind forcing. The modeling of the random wind excitation is described and the Peregrine breather solution for the case of constant wind is presented. Furthermore, the calculation of the corresponding water particle trajectories and hydrodynamic forces acting on cylindrical offshore structures is summarized. Afterward, results for the trajectories and forces for the case of no wind and random wind excitation are presented, respectively. Finally, this work ends with a conclusion.

Construction of the velocity potential

In order to compute the velocity potential of nonlinear water waves, the derivation of the NLS is sketched. Thereby, the Euler equations of fluid dynamics are simplified by using the method of multiple scales. Using the same approach, the corresponding water velocity potential can be computed, from which the water particle trajectories and hydrodynamic forces are calculated.

Formulation of the Euler equations

Water surface waves under the action of random wind and dissipation are considered. Let x and z denote the respective horizontal and vertical space variable and t the time variable. Only long-crested waves are considered propagating in the x-direction. The sea surface displacement is given by $z = \eta = \eta(x, t)$. Here, the still water position is located at $z = 0$ and it is assumed that the waves are not breaking, such that the value of η is uniquely defined. In addition, deep water waves on a sea with constant water depth $z = -h$ are considered.

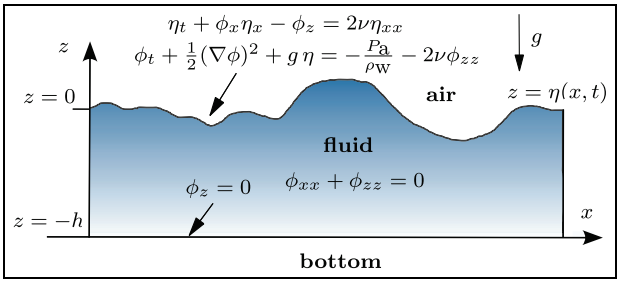

Figure 1. Governing equations of the nonlinear water wave problem.

Furthermore, it is assumed that the fluid is irrotational and incompressible. Then the corresponding velocity field of the water waves can be expressed in terms of the velocity potential $\phi(x, z, t)$. Denoting the wind-induced pressure at the sea surface by $P_a(x, z, t)$, the wind forced Euler equations of fluid dynamics can be written as[1]:

$$\phi_{xx} + \phi_{zz} = 0, \quad \text{for} \quad -h \leqslant z \leqslant \eta(x,t), \tag{1a}$$

$$\eta_t + \phi_x\eta_x - \phi_z = 2\nu\eta_{xx}, \quad \text{for} \quad z = \eta(x,t), \tag{1b}$$

$$\phi_t + \frac{1}{2}(\nabla\phi)^2 + g\,\eta = -\frac{P_a}{\rho_w} - 2\nu\phi_{zz}, \quad \text{for} \quad z = \eta(x,t), \tag{1c}$$

$$\phi_z = 0, \quad \text{for} \quad z = -h. \tag{1d}$$

Here, ∇ is the nabla operator in space. The variable ν denotes water kinematic viscosity, which is assumed to be small. The acceleration due to gravity is given by g and the constant density of water is ρ_w. The governing equations (1) are diagrammed in Figure 1. It should be noted that Dias et al.[1] derived the correction due to viscosity ν in the equations (1b) and (1c) by heuristic nonlinear generalizations of their linear versions.[12] However, there are several other proposals in the recent literature for the introduction of viscosity for water wave modeling, see for example the work of Wu et al.[13] Different types of similar viscous models have been compared by Eeltink et al.[14] However, the methodology presented in this paper remains the same for different types of viscosity modeling.

Derivation of the NLS

Since the nonlinear boundary conditions (1b) and (1c) are evaluated at the unknown sea surface displacement η, the computation of a numerical solution of the Euler equations is very inefficient, especially for the considered randomly forced nonlinear waves. In order to reduce the numerical effort, the method of multiple scales is used, which has for example been presented by

Nayfeh.[15] Following the approach of Davey and Stewartson,[16] the scalings

$$\xi := \varepsilon(x - c_g t), \quad \tau := \varepsilon^2 t \tag{2}$$

are used. Here, ε is a small parameter, which represents the wave steepness,

$$c_g := \frac{g}{2\omega}(\tanh(kh) + kh(1 - \tanh(kh)^2)) \tag{3}$$

is the group velocity, ω is the wave frequency of the considered carrier wave and $k = k(\omega)$ is the corresponding wave number, which follows from the dispersion relation $\omega^2 = kg\tanh(kh)$. Next, the surface displacement η and velocity potential ϕ are expanded in series of the form

$$\eta(x,t) = \sum_{n=1}^{\infty} \varepsilon^n \sum_{m=-n}^{n} \eta^{n,m}(\xi,\tau) e^{mi(kx-\omega t)}, \tag{4}$$

$$\phi(x,z,t) = \sum_{n=1}^{\infty} \varepsilon^n \sum_{m=-n}^{n} \phi^{n,m}(\xi,z,\tau) e^{mi(kx-\omega t)} \tag{5}$$

with

$$\eta^{(n,-m)} = \bar{\eta}^{(n,m)}, \qquad \phi^{(n,-m)} = \bar{\phi}^{(n,m)}. \tag{6}$$

Here, a bar denotes the complex conjugate.

The wind pressure is expanded by a similar series expansion as the surface displacement η and velocity potential ϕ. Following Leblanc,[7] the pressure P_a evaluated at $z = 0$ is expanded as

$$P_a(x,t) = \sum_{n=1}^{\infty} \varepsilon^n \sum_{m=-n}^{n} p^{n,m}(\xi,\tau) e^{mi(kx-\omega t)}. \tag{7}$$

In order to transform the nonlinear boundary conditions (1b) and (1c) to $z = 0$, a Taylor series expansion is applied. The expressions (4), (5), and (7) are substituted in the Euler equations with the transformed boundary conditions. Considering all terms up to order $\mathcal{O}(\varepsilon^3)$ and $h \to \infty$, the Euler equations reduce to the NLS[8]

$$i\psi_\tau - \frac{\omega}{8k^2}\psi_{\xi\xi} - \frac{1}{2}\omega k^2|\psi|^2\psi = -ik\frac{p^{1,1}}{\omega\rho w} - 2i\nu k^2\psi. \tag{8}$$

This is a partial differential equation for the wave envelope ψ, from which the surface displacement can be computed by

$$\eta(x,t) = \varepsilon \mathrm{Re}\{\psi(\xi(x,t),\tau(x,t))e^{i(kx-\omega t)}\} + \mathcal{O}(\varepsilon^2). \tag{9}$$

Here, $\mathrm{Re}\{y\}$ denotes the real part of y. Figure 2 shows an example of the wave envelope ψ together with the associated sea surface displacement η. It can be seen that

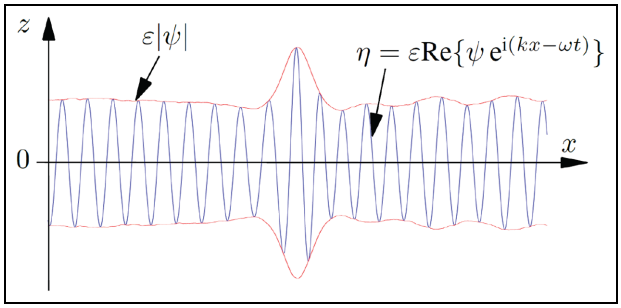

Figure 2. Example of the wave envelope ψ together with the associated sea surface displacement η.

while η changes with kx in space and with ωt in time, the wave envelope ψ changes only slowly in ξ and τ.

Modeling of random wind excitation

In order to model the random wind excitation as realistically as possible, the procedure of Dostal et al.[8] is followed, who use the Miles mechanism.[17,18] This mechanism has been proven to be a simple and versatile model for the calculation of wave growth in the presence of wind.[19] Following Dostal et al.[8] and Kharif et al.,[12] the wind pressure component $p^{1,1}$ is calculated by

$$p^{1,1}(\xi,\tau) = -\frac{\omega^2}{2g}\rho_a\beta\left(\frac{u_*(\xi,\tau)}{\kappa}\right)^2\psi(\xi,\tau). \tag{10}$$

Here, ρ_a is the density of air and κ is the von Kármán constant. The coefficient β and the friction velocity u_* are both described below. Inserting this in equation (8) and defining the forcing term

$$\Gamma(\xi,\tau) := \frac{\omega k}{2g}\frac{\rho_a}{\rho_w}\beta\left(\frac{u_*(\xi,\tau)}{\kappa}\right)^2 - 2\nu k^2, \tag{11}$$

the NLS reads

$$i\psi_\tau - \frac{\omega}{8k^2}\psi_{\xi\xi} - \frac{1}{2}\omega k^2|\psi|^2\psi = i\Gamma\psi. \tag{12}$$

In the derivation of equation (12), it has been assumed that the fluid viscosity ν and the density ratio ρ_a/ρ_w are small, that is, $\nu/\sqrt{g/k^3} = \mathcal{O}(\varepsilon^2)$, $\rho_a/\rho_w = \mathcal{O}(\varepsilon^2)$.[7,12] Given a logarithmic wind profile and a wind velocity $U(\xi,\tau,z)$ at height z, the friction velocity u_* can be computed by solving

$$U(\xi,z,\tau) = \frac{u_*(\xi,\tau)}{\kappa}\ln\left(\frac{z}{z_0}\right) \tag{13}$$

for u_*, where the roughness length is given by $z_0 = \alpha_{ch}u_*^2/g$ with the Charnock constant $\alpha_{ch} \approx 0.01875$.

As has been presented by Dostal et al.,[8] a CARMA(2,1)-process can be used to model $U(\xi, \tau, z)$ as a realistic stochastic wind process. Thereby, spectra of the wind velocity in the surface boundary layer are approximated, which have been measured by Van der Hoven.[20] By using this way of computation, wind gusts as well as wind fluctuations in the range of seconds to minutes can be modeled.

After computing u_* and following Conte and Miles,[21] the coefficient β can be calculated as a function of $\kappa c/\omega$, where c is the phase velocity of the wave. Thereby, the dimensionless roughness length $\kappa^2 g z_0/u_*^2$ has to be chosen. In all further calculations, the corresponding value is set to 0.003.

Initial conditions for the NLS

In order to compute numerical solutions of the NLS (12), corresponding initial conditions have to be chosen. In this work, the Peregrine breather is considered. This is an analytic solution of the NLS, which is localized in time and space. Therefore, the Peregrine breather describes a unique wave event in which large amplitude waves seem to come out of nowhere and disappear without a trace.[22] Thereby, the peak amplitude is several times higher than the background amplitude. It has been first found by Peregrine[23] for the unforced case $\Gamma = 0$. Later, using a Taylor series approximation of an exponential function, the solution found by Peregrine has been extended to the case of constant forcing Γ of small amplitude by Onorato and Proment.[24] The corresponding approximate solution of the NLS (12) is given by

$$\psi(\xi,\tau) = a_0 e^{\Gamma\tau} G(\xi,\tau) \times \left(\frac{4A(1 - \mathrm{i}2Ba_0^2 q(\tau)\tau)}{A + A(2Ba_0^2 q(\tau)\tau)^2 + 2Ba_0^2 (q(\tau)\xi)^2} - 1 \right), \tag{14}$$

with the free background amplitude parameter a_0 and

$$A = \frac{\omega}{8k^2}, B = \frac{1}{2}\omega k^2, \quad G(\xi,\tau) = \sqrt{q(\tau)}\, e^{\mathrm{i}\left(\Gamma q(\tau)/(2A) - Ba_0^2 q(\tau)\tau\right)}. \tag{15}$$

Here, the transformation $q(\tau) = 1/(1 - 2\Gamma\tau)$ is used, which has a singularity at $|2\Gamma\tau| = 1$. For $\Gamma = 0$, the solution (14) leads to the unforced solution presented by Peregrine.[23]

In different studies, it has been conjectured that the Peregrine is a prototype of rogue waves in the ocean.[8,25,26] One example of a measured rogue wave is the Draupner wave, which has been recorded on January 1st, 1995 in the central North Sea.[27] The remarkable height of the Draupner wave is 25.6 m. As has been shown, for example, by Chabchoub[28] and Witt,[6] the Peregrine model fits very well to the wave records of the Draupner wave, although it is just a single distorted uniform wave train solution.

Numerical solving of the NLS

In order to solve the NLS (12) numerically, the relaxation pseudo spectral scheme (ReSP)[29–31] is used. The time derivative is discretized by finite differences and a spectral approximation is performed in space using a discrete Fourier transform (DFT), whereby periodic boundary conditions in space are applied. In contrast to Crank–Nicolson-type schemes, the ReSP-method does not need to fulfill a Courant–Friedrichs–Lewy (CFL) condition, which links the discretization in time to the discretization in space and can make the numerical computation not feasible.

Using the ReSP-method, the NLS (12) is discretized by

$$\begin{aligned} \frac{\Lambda^{n+\frac{1}{2}} + \Lambda^{n-\frac{1}{2}}}{2} &= \frac{1}{2}\omega k^2 |\Psi^n|^2, \\ \mathrm{i}\frac{\Psi^{n+1} - \Psi^n}{\Delta\tau} &= \frac{\omega}{8k^2}\left(\frac{\Psi^{n+1} + \Psi^n}{2}\right)_{\xi\xi} \\ &\quad + \Lambda^{n+\frac{1}{2}}\frac{\Psi^{n+1} + \Psi^n}{2} \\ &\quad + \mathrm{i}\frac{\Gamma^{n+1}\Psi^{n+1} + \Gamma^n\Psi^n}{2}, \\ \Psi^0(\xi_j) = \psi_0(\xi_j), \Lambda^{-1/2}(\xi_j) &= \frac{1}{2}\omega k^2 |\Psi^0(\xi_j)|^2. \end{aligned} \tag{16}$$

Here, Ψ is a grid function with $\Psi_j^n = \Psi(\xi_j, \tau_n)$, which approximates the exact solution of the NLS ψ at the given grid points (ξ_j, τ_n), that is, $\Psi_j^n \approx \psi(\xi_j, \tau_n)$. Furthermore, ψ_0 is a given initial condition. Using the ReSP-method (16), the cubic nonlinearity of the NLS (12) is circumvented by an additional intermediate time step using the auxiliary variable Λ. Thus, it is not necessary to solve a nonlinear system of equations at each time step using the Newton-Raphson method.

The computation of the spatial derivatives is based on a DFT. In this way, an error due to the temporal discretization and Fourier approximation can not be avoided, but the spatial derivative is calculated accurately.

The presented ReSP-method (16) can be implemented such that a linear system of equations is solved in each time step. It is an implicit method, which is second-order accurate in time and spectrally accurate in space. Furthermore, it is unconditionally stable.[29]

Computation of particle trajectories and hydrodynamic forces

After calculating the numerical solution of the wind forced NLS (12), the corresponding sea surface displacement can be determined by equation (9). For the computation of the wave kinematics, particle trajectories and

hydrodynamic forces acting on a mechanical structure, the velocity potential ϕ has to be computed. Having determined a solution ψ of the NLS, Carter et al.[9] have shown that the velocity potential ϕ can be constructed in a similar way as the sea surface displacement η. Thereby, they have used the method of multiple scales and expanded ϕ in a similar way as presented in equation (5). It is noted that Carter et al.[9] have used the corresponding complex series expansions of equations (4) and (5), leading to the complex conjugated NLS for $\tilde{\psi} := 2\psi$. Using the transformations $X := \varepsilon x$ and $Z = :\varepsilon z$, the resulting velocity potential ϕ corresponding to the solution ψ of the NLS (12) reads

$$\begin{aligned}\phi(x,z,t) = \mathrm{Re}\Bigg\{\Bigg[&-\frac{\mathrm{i}\varepsilon\omega}{k}\hat{\psi} + \frac{\varepsilon^2\omega}{2k^2}\hat{\psi}_X \\ &+ \varepsilon^3\left(\frac{\mathrm{i}k\omega}{8}\hat{C} + \frac{3\mathrm{i}\omega}{8k^3}\hat{\psi}_{XX}\right)\Bigg]\times \\ e^{kz+\mathrm{i}(kx-\omega t)} &+ 2\varepsilon^2\phi_0 + 2\varepsilon^3\phi_1\Bigg\} + \mathcal{O}(\varepsilon^4).\end{aligned} \tag{17}$$

Equation (17) is the corrected version of the formula from Carter et al.,[9] whereby $\hat{\psi}(X,Z,\tau) := \psi(X-\mathrm{i}Z,\tau)$, $C := |\psi|^2\psi$, and $\hat{C}(X,Z,\tau) := C(X-\mathrm{i}Z,\tau)$. Furthermore, $\phi_0 = \phi_0(X,Z,\tau)$ and $\phi_1 = \phi_1(X,Z,\tau)$ are velocity potentials representing a mean flow of the water waves, whereby ϕ_0 can be computed as follows:

$$\mathrm{Re}\{2\phi_0\} = \phi_0 + \bar{\phi}_0 = \mathcal{F}^{-1}\left(\frac{1}{2}\mathrm{i}\omega\,\mathrm{sgn}(k)\mathcal{F}\left(|\psi|^2\right)\mathrm{e}^{|k|Z}\right). \tag{18}$$

Here, $\mathcal{F}(f)$ denotes the Fourier transform of the function f with respect to the coordinate X. As is shown at the end of this section, ϕ_1 is not needed for the computation of the particle paths and hydrodynamic forces and will therefore not be specified further at this point.

Since the numerical solution ψ is only known at the position X, the values of $\hat{\psi}(X,Z,\tau)$ and $\hat{C}(X,Z,\tau)$ have to be determined. This can be done by solving the complex transport equations

$$\begin{aligned}&\hat{\psi}_Z = -\mathrm{i}\hat{\psi}_X \text{ for } Z<0, \hat{\psi} = \psi \text{ at } Z = 0,\\ &\hat{C}_Z = -\mathrm{i}\hat{C}_X \text{ for } Z<0, \hat{C} = C \text{ at } Z = 0.\end{aligned} \tag{19}$$

Having computed the velocity potential, the corresponding velocity vector of a water particle located at (x,z) can be determined by calculating the gradient of ϕ. This results in

$$\begin{aligned}u(x,z,t) &= \frac{\partial\phi}{\partial x}(x,z,t),\\ v(x,z,t) &= \frac{\partial\phi}{\partial z}(x,z,t),\\ a(x,z,t) &= \frac{\partial u}{\partial t}(x,z,t),\end{aligned} \tag{20}$$

whereby u denotes the velocity in x-direction, v the velocity in z-direction and a the acceleration in x-direction, respectively.

With that, the trajectory $(x(t), z(t))$ of a water particle starting at $(x(0) = x_0, z(0) = z_0)$ can be calculated by

$$\frac{\mathrm{d}x}{\mathrm{d}t} = u(x(t),z(t),t), \frac{\mathrm{d}z}{\mathrm{d}t} = v(x(t),z(t),t). \tag{21}$$

Resulting from the computed wave kinematics, the hydrodynamic forces acting on mechanical structures can be determined. In order to compute the resulting loads on a cylindrical pile, the equation of Morison et al.[11] can be used, which considers the inertia and drag force. Denoting $\mathrm{d}F_x$ as the horizontal force acting on a part $\mathrm{d}z$ of a vertical pile with diameter D, the equation of Morison reads

$$\mathrm{d}F_x = C_\mathrm{m}\rho_\mathrm{w}\frac{\pi D^2}{4}\mathrm{d}za + C_\mathrm{d}\frac{\rho_\mathrm{w}}{2}D\mathrm{d}z|u|u. \tag{22}$$

Here, C_m is the inertia and C_d the drag coefficient, which can be determined by experiments. Integrating $\mathrm{d}F_x$ over the wetted surface of the cylindrical pile, the resulting hydrodynamic force F_x is computed.

Now it becomes clear why ϕ_1 is not needed for the computation of the particle paths and hydrodynamic forces: For the calculation of the particle paths and hydrodynamic forces, only the derivatives of ϕ with respect to the coordinates x, z and t are needed. However, ϕ_1 depends on the coordinates X, Z, and τ. Using $\varepsilon^3\phi_{1,x} = \varepsilon^4\phi_{1,X}$, $\varepsilon^3\phi_{1,z} = \varepsilon^4\phi_{1,Z}$, and $\varepsilon^3\phi_{1,t} = \varepsilon^5\phi_{1,\tau}$, the velocity potential ϕ_1 does contribute to the wave particle paths and hydrodynamic forces only at the order of $\mathcal{O}(\varepsilon^4)$. Since solutions of the Euler-equations (1) are approximated by the corresponding solution of the NLS up to an error of order $\mathcal{O}(\varepsilon^4)$, ϕ_1 can be neglected for the computation of wave particle paths and hydrodynamic forces.

Numerical results

In this section, the effects of random wind on a Peregrine breather are calculated. The water particle trajectories and hydrodynamic forces acting on a cylindrical pile are computed and compared with the case of the non-excited wave.

Solutions of the NLS are calculated by using the relaxation pseudo-spectral scheme, which has been presented in the last section. Periodic boundary conditions are assumed. As initial condition, the Peregrine breather is taken into account for the case of no wind forcing, that is, $\Gamma = 0$. For the computation of the hydrodynamic forces, a cylindrical pile of diameter $D = 6\,\mathrm{m}$ in a water depth of $h = 30\,\mathrm{m}$ is used. Here, the suggestion of Sarpkaya[32] is followed and the hydrodynamic coefficients C_m and C_d are set to $C_\mathrm{m} = 1.8$ and $C_\mathrm{d} = 0.64$, respectively. Moreover, the parameters $a_0 = 3\,\mathrm{m}$, $\omega = 1\,\mathrm{rad/s}$, $\varepsilon = 0.1$, $\rho_\mathrm{a} = 1.225\,\mathrm{kg/m^3}$, $\rho_\mathrm{w} = 1026.0\,\mathrm{kg/m^3}$, and $\nu = 10^{-2}\mathrm{cm^2/s}$ are used for

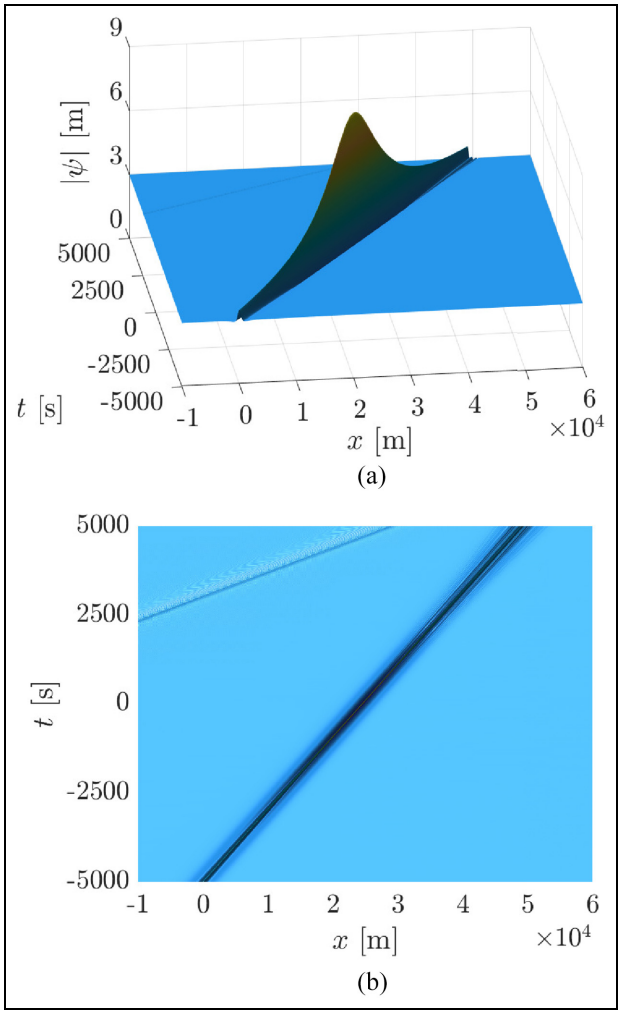

Figure 3. Temporal evolution of a Peregrine solution without wind forcing. The solution is shown (a) from the side and (b) from above.

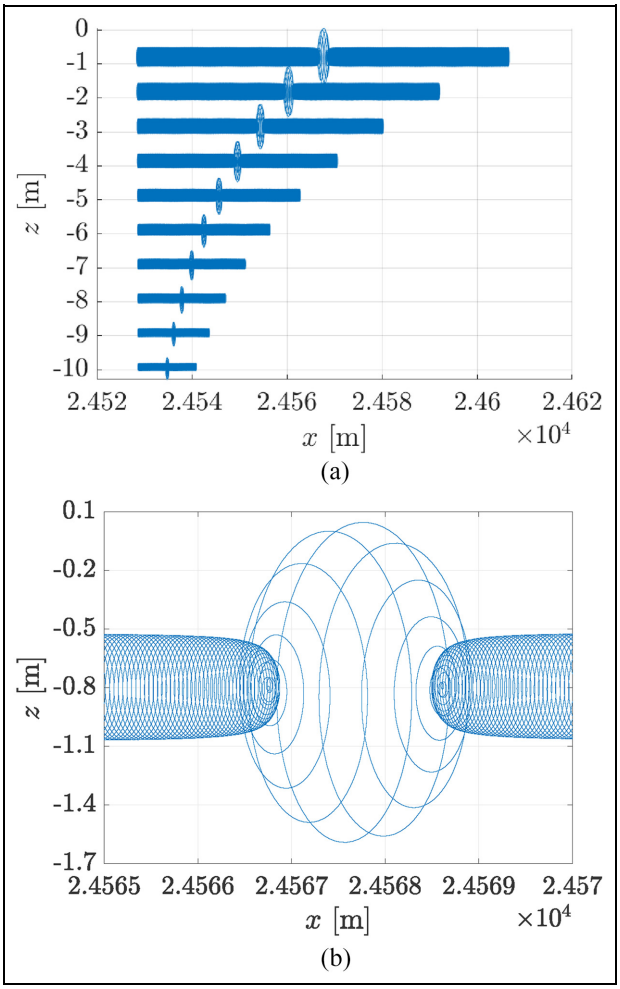

Figure 4. (a) Particle trajectories starting at $x_0 = 24529\,\mathrm{m}$ and heights going from $z_0 = -1\,\mathrm{m}$ to $z_0 = -10\,\mathrm{m}$ and (b) particle trajectory of a water particle starting at $(x_0, z_0) = (24529\,\mathrm{m}, -1\,\mathrm{m})$ in the time period $[-300\,\mathrm{s}, 300\,\mathrm{s}]$.

computations. A random wind velocity process with mean velocity $V_\mathrm{m} = 50\,\mathrm{km/h}$ at height $z = 50\,\mathrm{m}$ is considered, which is either time- or space-dependent. In both cases, the random wind process is constructed according to the method presented by Dostal et al.[8]

Peregrine breather without wind forcing

First, the case of a Peregrine breather without wind forcing is considered. Although the corresponding solution can be calculated analytically by using equation (14), the solution is computed numerically. In this way, the results of this subsection can later be better compared with the results for the case of wind excitation, since in both cases the effects of any occurring numerical errors are taken into account.

Figure 3 shows the temporal evolution of the unforced Peregrine breather from two different perspectives. It has to be noted that the spatial domain $[-12 \cdot 10^4\,\mathrm{m}, 12 \cdot 10^4\,\mathrm{m}]$ has been used in the numerical calculation and that only a part of the solution is shown in Figure 3. It can be seen that along the peak amplitude of the Peregrine breather solution, small errors are occurring in the upper left corner of Figure 3(b). They spread from the boundary of the spatial domain used for numerical calculations. This is due to the fact that although a relatively large spatial domain is taken into account, the computed Peregrine initial condition $\psi_0(x)$ provides no accurate periodic boundary condition in its spatial derivative, that is, $\psi_{0,x}(-12 \cdot 10^4\,\mathrm{m}) \neq \psi_{0,x}(12 \cdot 10^4\,\mathrm{m})$. The spatial domain is chosen such that the disturbance coming from the boundary does not affect the Peregrine solution. However, in order to save computation time, the boundary is not big enough such that the disturbance is still visible in the results.

Knowing ψ, the particle trajectories and hydrodynamic forces acting on a cylindrical pile can be computed using the approach described in the last section. Figure 4(a) shows the trajectories of particles starting at $x_0 = 24529\,\mathrm{m}$ and heights going from $z_0 = -1\,\mathrm{m}$ to $z_0 = -10\,\mathrm{m}$. With the chosen value for x_0, the particles are starting at the x-position where the Peregrine breather reaches its maximal peak amplitude. For the

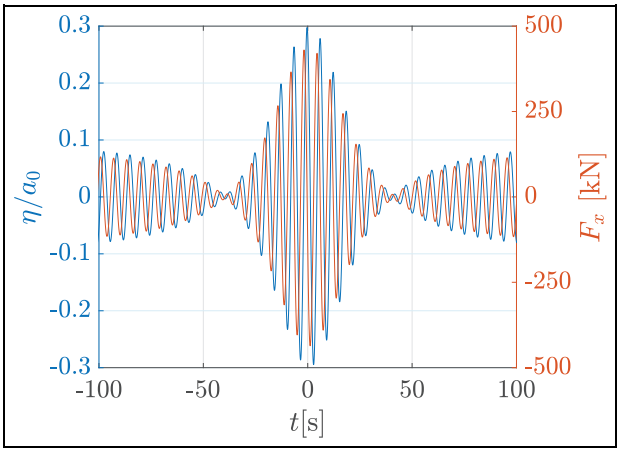

Figure 5. Sea Surface displacement (blue) and hydrodynamic forces (orange) acting on a cylindrical pile, resulting from a Peregrine breather without the presence of wind.

background waves of the Peregrine solution, the particles move on ellipsoidal orbits with a drift in the positive x-direction. As can be seen, this horizontal drift decays exponentially in z. When the water particle is reached by the peak amplitude of the Peregrine breather, the ellipsoidal paths get larger. Figure 4(b) presents a particle trajectory of the water particle starting at $(x_0, z_0) = (24529\,\text{m}, -1\,\text{m})$ in the time interval $[-300\,\text{s}, 300\,\text{s}]$, in which the particle reaches the peak amplitude of the Peregrine solution.

For a submerged cylindrical pile located at $x_0 = 24529\,\text{m}$, the acting hydrodynamic forces are shown in Figure 5 in the time interval $[-100\,\text{s}, 100\,\text{s}]$. Furthermore, the corresponding sea surface displacement $\eta(x_0, t)$ is presented. Compared to the carrier wave, the force and sea surface displacement are multiplied by a factor of approximately three when the cylindrical pile is hit by the maximal peak amplitude of the Peregrine solution. Moreover, it is shown that the sea surface and hydrodynamic forces are shifted over time. When the cylindrical pile is not reached by the peak amplitude of the Peregrine solution, the phase difference is about 88°. However, due to the nonlinearity of the Peregrine solution, this phase difference changes when the peak amplitude of the Peregrine solution reaches the cylindrical pile. The phase shift comes due to the fact that the forces depend on the velocity and acceleration of the water particles given by equation (17). The derivatives of ϕ are time-shifted to the sea surface displacement η given by equation (9).

The effects of time-dependent wind forcing

In this subsection, the effects of time-dependent wind forcing on the particle trajectories and hydrodynamic forces are studied. For this, a random wind velocity at height $z = 50\,\text{m}$ with mean velocity $V_\text{m} = 50\,\text{km/h}$ is simulated using the method described by Dostal et al.[8] An example of such a random wind process as well as

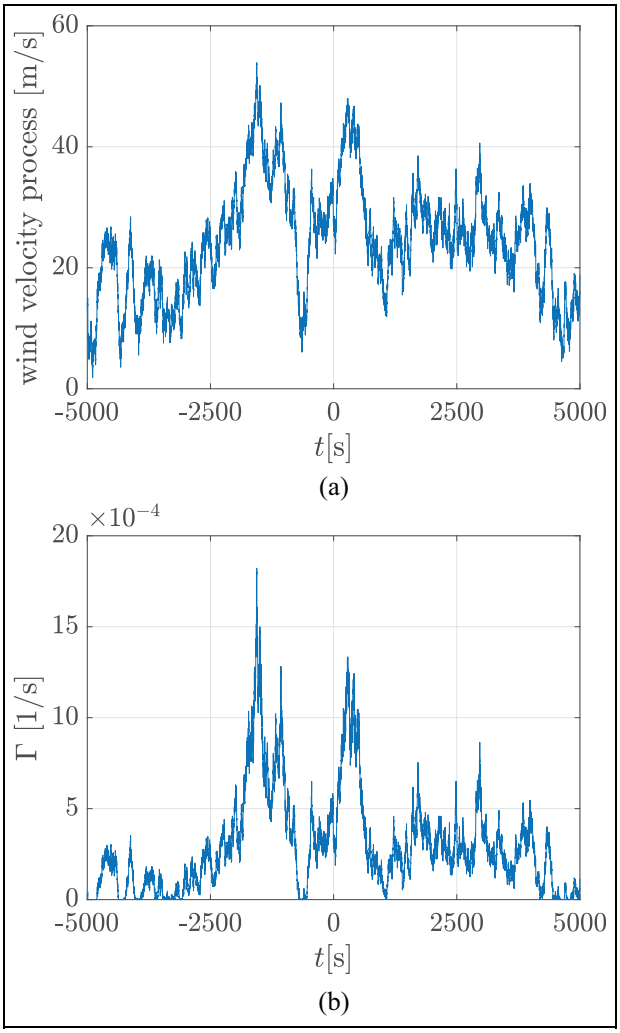

Figure 6. (a) Time-dependent random wind velocity and (b) corresponding excitation Γ.

the corresponding excitation Γ is shown in Figure 6. The resulting numerical solution of the NLS (12) is presented in Figure 7 from two different perspectives. Although small fluctuations in the amplitude can be observed, it is shown that the Peregrine breather can be clearly identified even under strong and gusty wind conditions.

In order to investigate the effects of random wind, Figure 8 compares the particle trajectory and hydrodynamic force with the corresponding results for the case of no wind forcing. Again, a water particle starting at $(x_0, z_0) = (24529\,\text{m}, -1\,\text{m})$ and a cylindrical pile located at $x_0 = 24529\,\text{m}$ are considered. Figure 8(a) presents the particle trajectories in the spatial domain $[24565\,\text{m}, 24570\,\text{m}]$ and Figure 8(b) the corresponding hydrodynamic forces. Furthermore, the maximal amplitudes of the forces resulting from the carrier wave of the Peregrine breather solutions are shown in Figure 8(c). It can be seen that due to the random wind forcing, the temporal behavior of the particle trajectory stays the same, but it experiences a larger drift in x-direction. Compared to the case without wind forcing, this leads

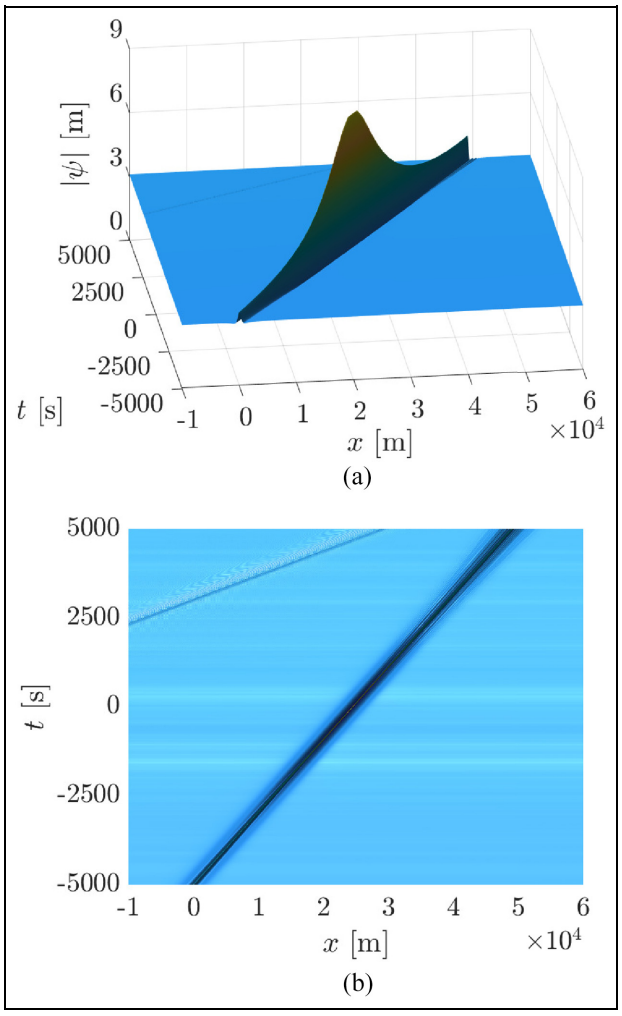

Figure 7. Temporal evolution of a Peregrine solution with time-dependent wind forcing. The solution is shown (a) from the side and (b) from above.

to a slight increase of the amplitude of the hydrodynamic force over time of about 3%. It has to be noted that the disturbance of the forces at the end of the considered temporal period comes from numerical errors, which have been described in the last section.

This shows that the Peregrine breather also appears under time-dependent realistic wind forcing and that the wind leads to slightly higher hydrodynamic forces.

The effects of space-dependent wind forcing

Finally, the effects of space-dependent wind forcing on the particle trajectories and hydrodynamic forces are studied. A random wind velocity at height $z = 50\,\mathrm{m}$ with mean velocity $V_\mathrm{m} = 50\,\mathrm{km/h}$ is simulated. An example of a space-dependent wind velocity as well as the corresponding excitation Γ is presented in Figure 9. The resulting numerical solution of the NLS (12) is shown in Figure 10. Again, small fluctuations can be observed. But in contrast to the case of a time-dependent wind forcing, these fluctuations are varying

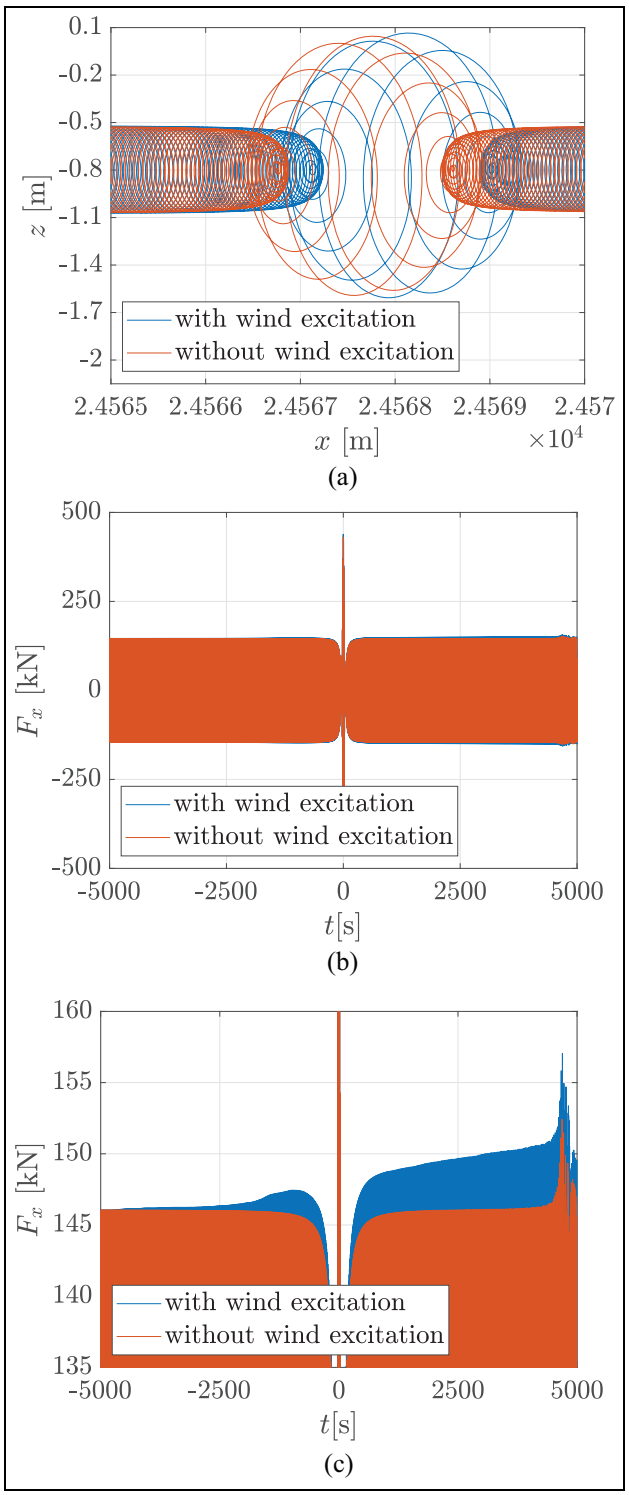

Figure 8. Particle trajectories and hydrodynamic forces for the case of time-dependent (blue) wind forcing and no wind forcing (orange): (a) trajectories of particles starting at $(x_0, z_0) = (24529\,\mathrm{m}, -1\,\mathrm{m})$, (b) hydrodynamic force amplitudes due to the Peregrine breather, which acts on a pile located at $x_0 = 24529\,\mathrm{m}$, and (c) zoom in (b) at the maximal hydrodynamic force amplitudes due to the background wave of the Peregrine breather.

in space. However, the Peregrine breather can again be clearly identified.

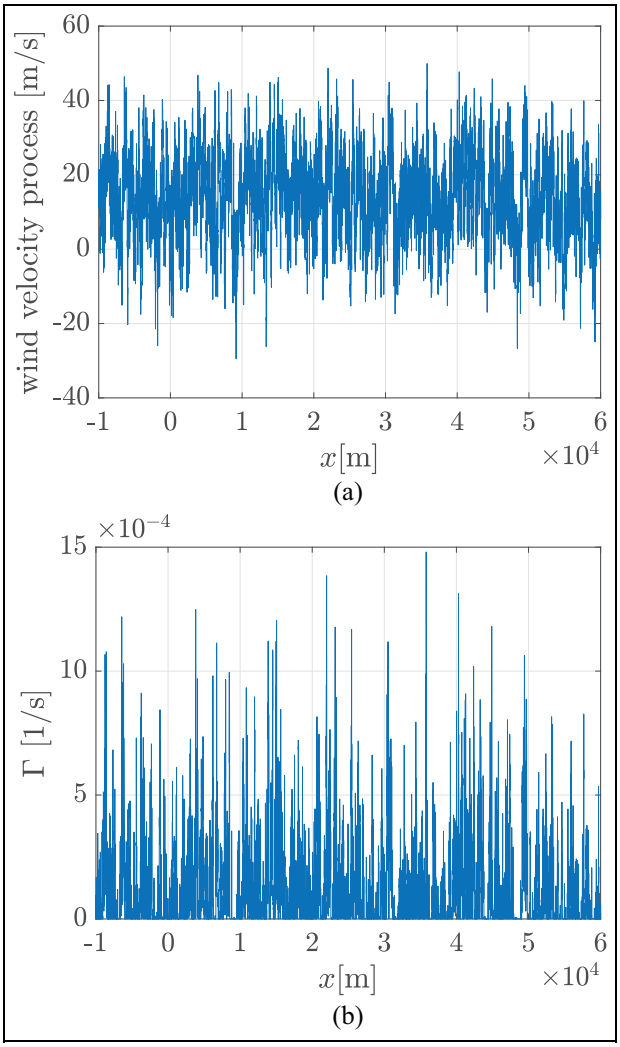

Figure 9. (a) Space-dependent random wind velocity and (b) corresponding excitation Γ.

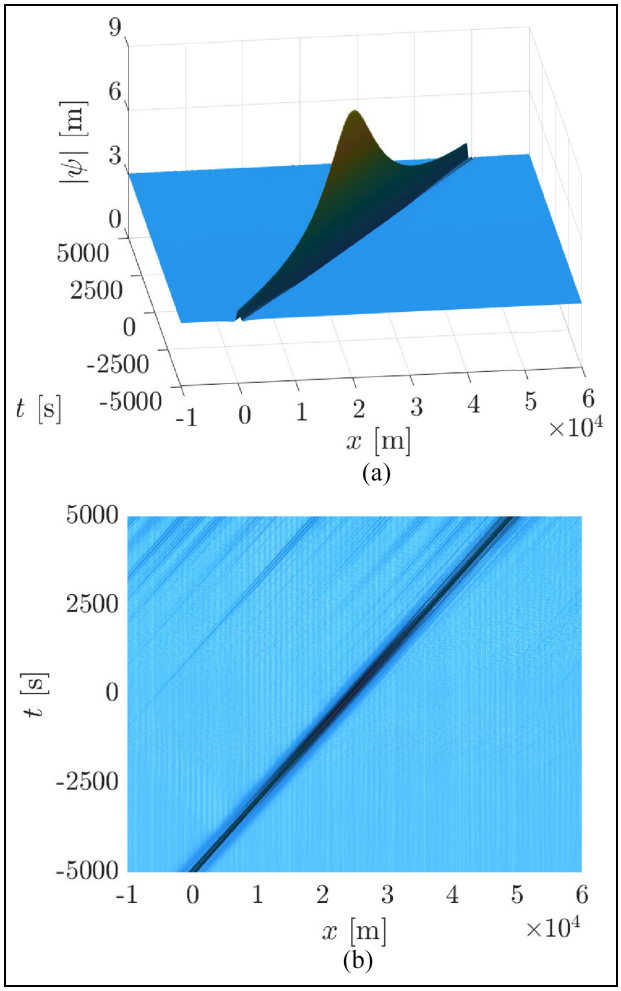

Figure 10. Temporal evolution of a Peregrine solution with space-dependent wind forcing. The solution is shown (a) from the side and (b) from above.

In order to study the effect of the space-dependent wind on the water particle trajectories, Figure 11(a) presents the trajectory of a particle starting at $(x_0, z_0) = (24529\,\text{m}, -1\,\text{m})$. Figure 11(b) shows the corresponding hydrodynamic forces on a cylindrical pile located at $x_0 = 24529\,\text{m}$. Furthermore, the maximal amplitudes of the forces resulting from the background wave of the Peregrine breather are shown in Figure 11(c). Again it can be seen that a wind excitation leads to a horizontal shift of the particle trajectory. Moreover, it is depicted that a space-dependent wind leads to a maximal force amplitude, which is increasing with time. However, in contrast to the amplitude of the force resulting from a time-dependent wind excitation, this increase is smaller and includes higher time-dependent fluctuations.

It can be concluded that the Peregrine breather also appears under space-dependent realistic wind forcing, which leads to an increasing hydrodynamic force. Thereby, in the space-dependent case the maximal force amplitude experiences higher temporal fluctuations than in the case of time-dependent wind forcing.

Conclusion

The influence of time- and space-dependent random wind forcing on nonlinear ocean waves is studied by investigating the corresponding hydrodynamic forces acting on cylindrical offshore structures. The used approach is based on solutions of the NLS as well as on the theory of Carter et al.,[9] which provides the corresponding velocity potential. The hydrodynamic forces are computed using the equation of Morison. Results are presented for the Peregrine breather solution of the NLS.

It is shown that the Peregrine solution can clearly be identified in the presence of a strong time- and space-dependent wind excitation, respectively. However, both cases of wind forcing lead to a larger drift of the water particles in the horizontal direction. Considering cylindrical offshore structures, wind forcing results in a slightly increased hydrodynamic force. For a mean wind velocity of $V_\text{m} = 50\,\text{km/h}$ an increase of the force amplitude of about 3% is observed. Moreover, space-dependent wind forcing leads to small fluctuations in the hydrodynamic force amplitudes.

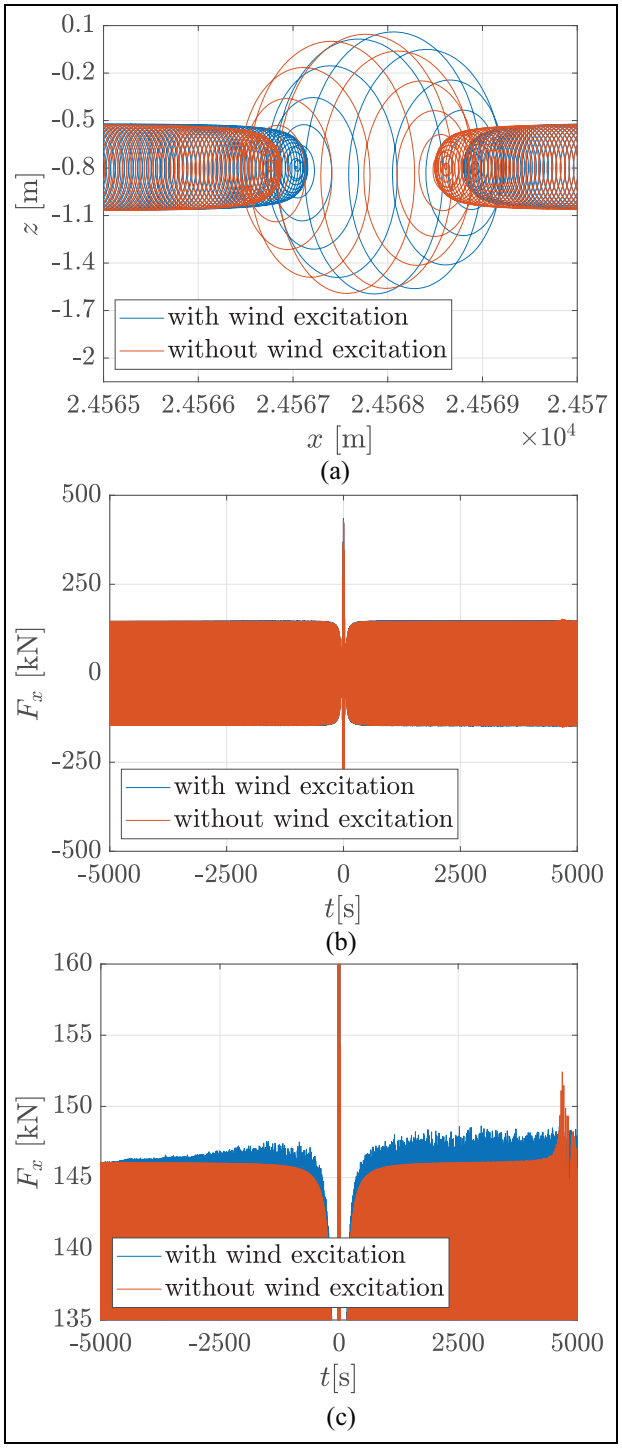

Figure 11. Particle trajectories and hydrodynamic forces for the case of space-dependent (blue) wind forcing and no wind forcing (orange): (a) trajectories of particles starting at $(x_0, z_0) = (24529\,\text{m}, -1\,\text{m})$, (b) hydrodynamic force amplitudes due to the Peregrine breather, which acts on a pile located at $x_0 = 24529\,\text{m}$, and (c) zoom in (b) at the maximal hydrodynamic force amplitudes due to the background wave of the Peregrine breather.

Therefore, it can be concluded that the Peregrine breather can exist in the presence of random wind forcing. However, the wind forcing leads to small changes in the occurring hydrodynamic force amplitudes, which should be considered for the construction of cylindrical offshore structures, like jacket structures and piles, operating in the ocean.

Declaration of conflicting interests

The author(s) declared no potential conflicts of interest with respect to the research, authorship, and/or publication of this article.

Funding

The author(s) received no financial support for the research, authorship, and/or publication of this article.

ORCID iD

Marten Hollm https://orcid.org/0000-0001-5139-8918

References

1. Dias F, Dyachenko AI and Zakharov VE. Theory of weakly damped free-surface flows: a new formulation based on potential flow solutions. *Phys Lett A* 2008; 372(8): 1297–1302.
2. Zakharov VE. Stability of periodic waves of finite amplitude on the surface of a deep fluid. *J Appl Mech Tech Phys* 1972; 9(2): 190–194.
3. Osborne AR. *Nonlinear ocean waves and the inverse scattering transform*. San Diego, CA: Academic Press, 2010.
4. Onorato M, Residori S, Bortolozzo U, et al. Rogue waves and their generating mechanisms in different physical contexts. *Phys Rep* 2013; 528(2): 47–89.
5. Fedele F, Brennan J, Ponce de León S, et al. Real world ocean rogue waves explained without the modulational instability. *Sci Rep* 2016; 6(1): 27715–27811.
6. Witt A. *Inducing predefined nonlinear rogue waves on basis of breather solutions*. PhD thesis, Hamburg University of Technology, 2019.
7. Leblanc S. Amplification of nonlinear surface waves by wind. *Phys Fluids* 2007; 19(10): 101705.
8. Dostal L, Hollm M and Kreuzer E. Study on the behavior of weakly nonlinear water waves in the presence of random wind forcing. *Nonlinear Dyn* 2020; 99(3): 2319–2338.
9. Carter JD, Curtis CW and Kalisch H. Particle trajectories in nonlinear Schrödinger models. *Water Waves* 2020; 2(1): 31–57.
10. Hollm M, Dostal L and Seifried R. Particle paths and hydrodynamic forces of random wind forced nonlinear ocean waves. In: Ergin S and Soares CG (eds) *Sustainable Development and innovations in Marine Technologies*. London: CRC Press, 2022, pp.51–58.
11. Morison JR, Johnson JW and Schaaf SA. The force exerted by surface waves on piles. *J Pet Technol* 1950; 2(05): 149–154.
12. Kharif C, Kraenkel RA, Manna MA, et al. The modulational instability in deep water under the action of wind and dissipation. *J Fluid Mech* 2010; 664: 138–149.
13. Wu G, Liu Y and Yue DKP. A note on stabilizing the Benjamin–Feir instability. *J Fluid Mech* 2006; 556: 45–54.

14. Eeltink D, Armaroli A, Brunetti M, et al. Reconciling different formulations of viscous water waves and their mass conservation. *Wave Motion* 2020; 97: 102610.
15. Nayfeh AH. *Perturbation methods*. Hoboken; NJ: John Wiley & Sons.
16. Davey A and Stewartson K. On three-dimensional packets of surface waves. *Proc R Soc Lond A Math Phys Sci* 1974; 338(1613): 101–110.
17. Miles JW. On the generation of surface waves by shear flows. *J Fluid Mech* 1957; 3(02): 185–204.
18. Miles JW. On the generation of surface waves by shear flows. Part 2. *J Fluid Mech* 1959; 6(4): 568–582.
19. Hristov TS, Miller SD and Friehe CA. Dynamical coupling of wind and ocean waves through wave-induced air flow. *Nature* 2003; 422(6927): 55–58.
20. Van der Hoven I. Power spectrum of horizontal wind speed in the frequency range from 0.0007 to 900 cycles per hour. *J Meteorol* 1957; 14(2): 160–164.
21. Conte SD and Miles JW. On the numerical integration of the Orr-Sommerfeld equation. *J Soc Ind Appl Math* 1959; 7(4): 361–366.
22. Chabchoub A, Akhmediev N and Hoffmann NP. Experimental study of spatiotemporally localized surface gravity water waves. *Phys Rev E* 2012; 86(1): 016311.
23. Peregrine DH. Water waves, nonlinear Schrödinger equations and their solutions. *ANZIAM J* 1983; 25(1): 16–43.
24. Onorato M and Proment D. Approximate rogue wave solutions of the forced and damped nonlinear Schrödinger equation for water waves. *Phys Lett A* 2012; 376(45): 3057–3059.
25. Dysthe KB and Trulsen K. Note on breather type solutions of the NLS as models for freak-waves. *Phys Scr* 1999; 1999(T82): 48.
26. Shrira VI and Geogjaev VV. What makes the peregrine soliton so special as a prototype of freak waves? *J Eng Math* 2010; 67: 11–22.
27. Adcock TAA, Taylor PH, Yan S, et al. Did the draupner wave occur in a crossing sea? *Proc R Soc A Math Phys Eng Sci* 2011; 467(2134): 3004–3021.
28. Chabchoub A. *An experimental study on breathers in water waves*. PhD thesis, Hamburg University of Technology, 2013.
29. Antoine X, Bao W and Besse C. Computational methods for the dynamics of the nonlinear schrödinger/gross–pitaevskii equations. *Comput Phys Commun* 2013; 184(12): 2621–2633.
30. Antoine X and Duboscq R. Gpelab, a matlab toolbox to solve gross–pitaevskii equations ii: Dynamics and stochastic simulations. *Comput Phys Commun* 2015; 193: 95–117.
31. Antoine X and Duboscq R. Modeling and computation of Bose-Einstein condensates: stationary states, nucleation, dynamics, stochasticity. In: Besse C and Garreau JC (eds) *Nonlinear optical and atomic systems*. Cham: Springer, 2015, pp.49–145.
32. Sarpkaya T. Vortex shedding and resistance in harmonic flow about smooth and rough circular cylinders at high Reynolds numbers. Technical report, Naval Postgraduate School, Monterey, CA, 1976.

Appendix

Notation

a	acceleration in x-direction
a_0	background amplitude of Peregrine solution
A	parameter of Peregrine solution
B	parameter of Peregrine solution
c_g	group velocity
C	auxiliary variable in velocity potential ϕ
C_d	drag coefficient
C_m	inertia coefficient
D	diameter of cylindrical pile
F_x	force in x-direction
g	acceleration due to gravity
G	parameter of Peregrine solution
h	water depth
k	wave number
P_a	wind-induced pressure
q	parameter of Peregrine solution
t	time coordinate
u	velocity in x-direction
u_*	friction velocity
U	wind velocity
v	velocity in z-direction
V_m	mean wind velocity
x	horizontal space coordinate
X	scaled horizontal coordinate
z	vertical space coordinate
z_0	roughness length
Z	scaled vertical coordinate
α_{ch}	Charnock constant
β	coefficient for Miles mechanism
Γ	forcing term
ε	wave steepness
η	sea surface displacement
κ	von Kármán constant
Λ	auxiliary variable in ReSP-method
ν	kinematic viscosity
ξ	scaled space coordinate
ξ_j	grid point in space
ρ_a	density of air
ρ_w	density of water
τ	scaled time coordinate
τ_n	grid point in time
ϕ	velocity potential
ϕ_0	first mean velocity potential
ϕ_1	second mean velocity potential
ψ	wave envelope
ψ_0	initial condition for ReSP-method
Ψ	grid function
ω	wave frequency